CERES Cloud Properties Derived From Multispectral VIRS Data

Patrick Minnis[a], David F. Young[a], Bruce A. Wielicki[a], Patrick W. Heck[b], Xiquan Dong[c],
Larry L. Stowe[d], and Ronald Welch[e]

[a]NASA Langley Research Center, MS 420, Hampton, VA, USA 23681
[b]AS&M, Inc., Hampton, VA, USA
[c]Department of Meteorology, University of Utah, USA
[d]NOAA/NESDIS, Camp Springs, MD, USA
[e]University of Alabama in Huntsville, USA

ABSTRACT

The Clouds and Earth's Radiant Energy System (CERES) experiment, the first satellite project devoted to monitoring cloud macrophysical and microphysical properties simultaneously with the broadband radiation field, is designed to dramatically improve our understanding of the relationship between clouds and the Earth's radiation budget. The first CERES instruments flew on the Tropical Rainfall Measuring Mission (TRMM) satellite between 35°N and 35°S with the Visible Infrared Scanner (VIRS), a 2-km resolution imager with five channels: 0.65, 1.6, 3.75, 10.8, and 12 µm beginning in January 1998. Cloud amount, height, temperature, phase, effective particle size, and water path are derived from the VIRS radiances and validated using surface radar and lidar data. Droplet radii are largest over ocean and smallest over land. Mean droplet radius is larger than that from earlier studies. The mean ice diameter is 61 µm. Variations of cloud parameters with temperature and viewing and solar zenith angle are given. Surface observations of liquid water path and droplet size agree well with the VIRS retrievals. This is the first analysis of cloud microphysical properties covering all times of day using all available pixels and viewing angles for half of the globe. Seasonal and diurnal variations of the cloud properties are presented.

Keywords: clouds, CERES, VIRS, TRMM, cloud microphysics, diurnal cycle, water path, climate, radiation, remote sensing

1. INTRODUCTION

Accurate measurement of the Earth's radiation budget and understanding of its interaction with various components of the atmosphere and surface requires reliable determination of the scene constituents. The Clouds and the Earth's Radiant Energy System (CERES) Project is meeting this need by simultaneously observing relatively low-resolution broadband radiances and high-resolution imager narrowband radiances[1]. The latter are used to classify the scene while the former provide the radiation budget measurements. The scene classifications are used to help develop and select bidirectional reflectance models appropriate for the scene. Identification of the atmospheric state of each pixel facilitates further quantification of surface, aerosol, or cloud properties. Once identified as cloudy, the pixel radiances can be analyzed to determine the properties of clouds in the field of view.

Cloud microphysical properties such as effective particle size, phase, and optical depth and macrophysical properties such as altitude and fractional coverage provide the critical links between the hydrological cycle and the effect of clouds on the radiation budget. This paper briefly describes the methodology of the CERES daytime cloud property retrieval subsystem and presents the initial results of its application to the fully calibrated, 2-km resolution Visible and Infrared Scanner (VIRS) on the 35°-inclined-orbit Tropical Rainfall Measuring Mission (TRMM) satellite. One of the unique features of the TRMM satellite is its complete diurnal sampling pattern which permits the determination of cloud and surface properties over a given surface type over all times of day. The distributions of cloud phase, effective particle sizes, liquid water path, ice water path, heights, and fractional coverage are derived from January, February, and April 1998 data.

2. DATA

The VIRS satellite measures radiances at 0.65, 1.6, 3.75, 10.8, and 12.0 µm in a cross-track scan out to a nadir angle of 45°, which translates to a maximum viewing zenith angle θ of 48°. The TRMM orbit gives the VIRS a viewing perspective distinctly different from either geostationary or Sun-synchronous satellites and allows it to sample all local times of day over a 46-day period. At the Equator, this sampling is evenly distributed over the period, but at higher latitudes, the sampling is primarily in darkness for 3 weeks followed by 3 weeks of sunlight. Each pixel is ultimately classified as clear or cloudy. Cloudy pixels are then analyzed to determine the average properties of the cloud in the pixel.

Predictions of clear radiances and their uncertainties are required to discriminate between clear and cloudy scenes and are used in the calculations of cloud properties. Although the clear radiances are estimated differently for each channel, each radiance must be specified for a given latitude λ, longitude ϕ, time of day t, month m, solar zenith angle θ_o, θ, and relative azimuth angle ψ. Clear-sky radiances are predicted at a 10' latitude-longitude resolution, but are often only defined on a 1° grid. Each 10' box is defined as water, permanent snow, or land and has a mean surface elevation $z_s(\lambda,\phi)$ associated with it. Clear-sky albedo maps, directional reflectance models, and bidirectional reflectance functions are used to predict expected clear-sky reflectances for the 0.65, 1.6, and 3.75-µm channels[2]. The maps also include spatial and temporal standard deviations of the reflectances and variability within a 10' box. Surface elevation, vegetation type, snow coverage maps, and vertical profiles of temperature and humidity are all included in the analysis procedures. Surface skin temperatures from numerical weather analyses and empirical spectral surface emissivities are used to compute top-of-atmosphere brightness temperatures at 3.75, 10.8, and 12.0 µm.

The channels-1 (VIS) clear-sky and -2 (NIR) surface reflectance is

$$\rho_1 = \alpha_1(\lambda,\phi,m) \ \delta_1(\theta_o) \ \chi_1(\theta_o,\theta,\Psi), \qquad\qquad (1)$$

where α_1 is the overhead-sun albedo, δ_1 is the normalized directional reflectance model, and χ_1 is the bidirectional distribution function. Except for ocean, the values of δ_1 are defined[2] for each of 19 IGBP (International Geosphere Biosphere Programme) surface types k.

The clear-sky albedos and directional models for ocean are derived from an updated version of a clear ocean model[3]. The overhead-sun albedos for all other areas were taken from maps created using an initial pass through the VIRS data with the following procedure[2]. Clear reflectances in a given 10' region are converted to α_1 using (1) and used to compute the mean and standard deviation for each pass during the month. The relative rms average $\sigma_1(\lambda,\phi,m)$ of the temporal and spatial standard deviations is normalized to $<\alpha_1>$ to obtain the basic uncertainty in a given value of $<\alpha_1>$. Mean values of α_1 (k,m) and $\sigma_1(k,m)$ are then computed from the regions having clear data. The results for each month are filtered to eliminate poor sampling. All unfilled regions are then assigned the appropriate $\alpha_1(k,m)$ and $\sigma_1(k,m)$. In application, (1) is solved using the filled dataset. If the observed clear-sky reflectances from the second pass through the VIRS data differ substantially from the initial results in a given 10' box, the albedo is updated to reflect the new observations. The result is a much more realistic 10' overhead visible albedo.

The 1.6-µm albedos are also based on an initial pass through the VIRS data[2]. The surface reflectances are computed in a fashion similar to (1) then adjusted to the top of the atmosphere (TOA) by accounting for gaseous absorption. These results are also updated when the observed values differ significantly from the original predicted values. Figure 1a shows the VIS clear-sky albedos derived using January 1987 NOAA-9 Advanced Very High Resolution Radiometer (AVHRR) data from the clear-sky ISCCP DX (ISCCP refers to the International Satellite Cloud Climatology Project) data on a 1° grid and updated to a 10' grid with January 1998 VIRS data. The 1.6-µm overhead surface albedos derived from VIRS are shown in Figure 1b. Values poleward of 37° are filled with mean values for the dominant IGBP type in each 10' box. The VIS albedos are generally much smaller than the NIR albedos except for snow and water where the opposite relationship is observed.

The 3.7-µm (SIR) radiance leaving the surface is approximated as

$$B_3(T_{s3}) = \varepsilon_3\{B_3(T_{skin})\} + \alpha_3 \ \delta_3(\theta_o) \ \chi_3 S_3', \qquad\qquad (2)$$

where B_3 is the Planck function, T_{skin} is the surface skin temperature, ε_3 is the surface emissivity, T_{s3} is the apparent surface temperature at 3.7 µm, and S_3' is the solar radiation incident at the surface. $B_3(T_{s3})$ is then corrected for attenuation by the atmosphere to predict the clear-sky temperature T_{cs3}. The surface emissivities for channels 3, 4, and 5 were derived from the clear-sky ISCCP DX data on a 1° grid using the method described by Minnis et al.[4]. Means and standard deviations are computed and all 1° regions with no values are filled using the IGBP-type averages. The values of δ_3 and χ_3 are specified

using δ_1 and χ_1, respectively. This approach yields a mean difference between the observed and predicted values of T_{cs3} of –2 to +2K and –1 to +1K during daytime and nighttime, respectively, with standard deviations σ_3 less than 3K and 2K.
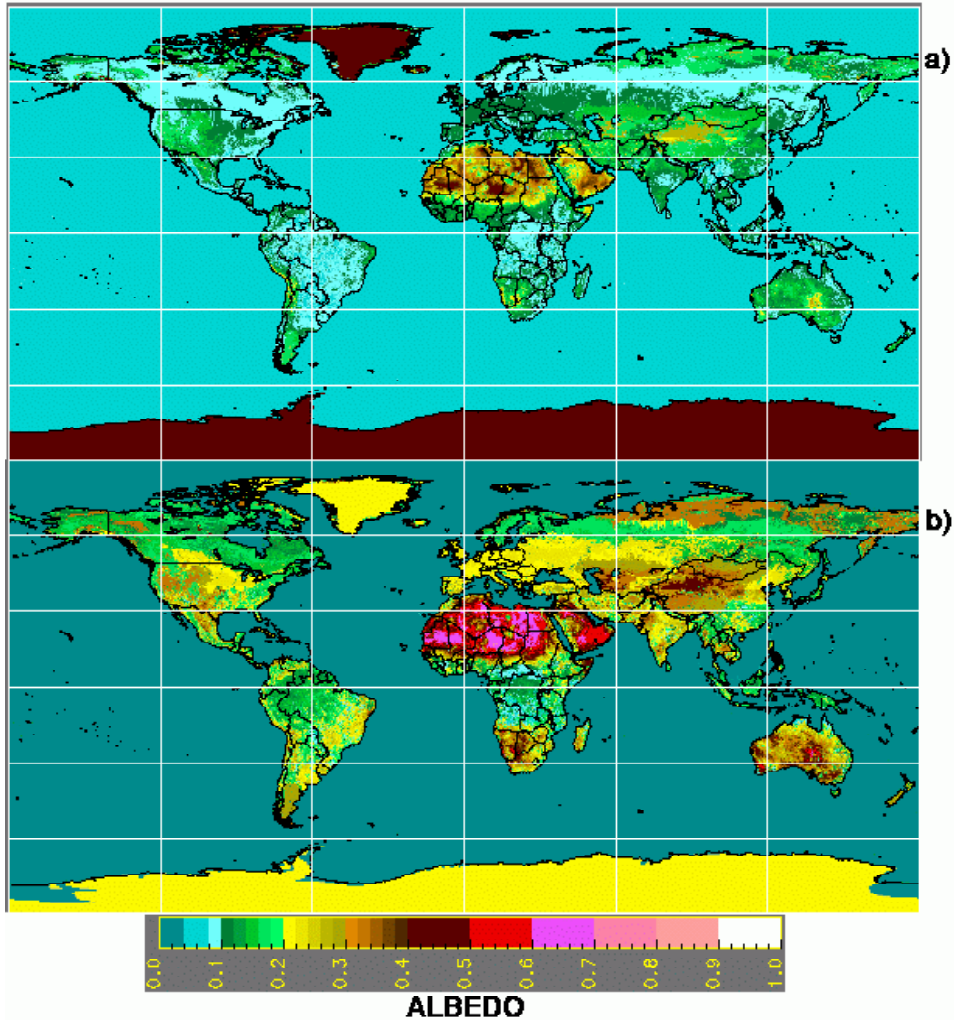

Figure 1. Albedos at $\theta_o = 0°$ for January 1998 from VIRS, a) clear-sky 0.65 µm and b) surface 1.6 µm.

The 10.8 and 12.0-µm TOA temperatures are derived from 3-hourly skin temperatures computed by a numerical weather analysis model and corrected for temporal phase lags and the surface emissivity, then adjusted to the TOA by accounting for gaseous absorption and emission of the atmosphere. Clear-sky temperature uncertainties are estimated as the standard deviations between the predicted and observed temperatures with minima of 2.5 and 3.0K for ocean and land, respectively.

3. CLOUD MASK

The CERES scene classification technique consists primarily of cascading threshold tests. To define a pixel as cloudy, at least one of its five spectral radiances must differ significantly from the corresponding expected clear-sky radiances. A cloudy pixel may be classified as strong or weak depending on how much the radiances differ from the predicted clear-sky radiances. Pixels identified as clear are designated as weak or strong or categorized as being filled with smoke, fire, or aerosol, contaminated by sunglint, or covered with snow. The daytime ($\theta_o < 78°$) masking algorithm can use all five channels, while the nighttime technique only employs channels 3, 4, and 5.

3.1 Daytime mask

Every pixel is classified during daylight using a sequence of tests. The first check, or **A** test, identifies all pixels that are obviously too cold to be cloud free. If $T_4 < T_A$, then the pixel is designated a strong cloud. The value of T_A is equal to the temperature at 500 mb over land or to $T_{skin} - 10K$ over ocean. If the pixel is not cloudy after the **A** test, it is then

compared against the expected clear-sky radiances in the following **B** tests, where the parameters *B1*, *B2*, and *B3* are initialized to 0.

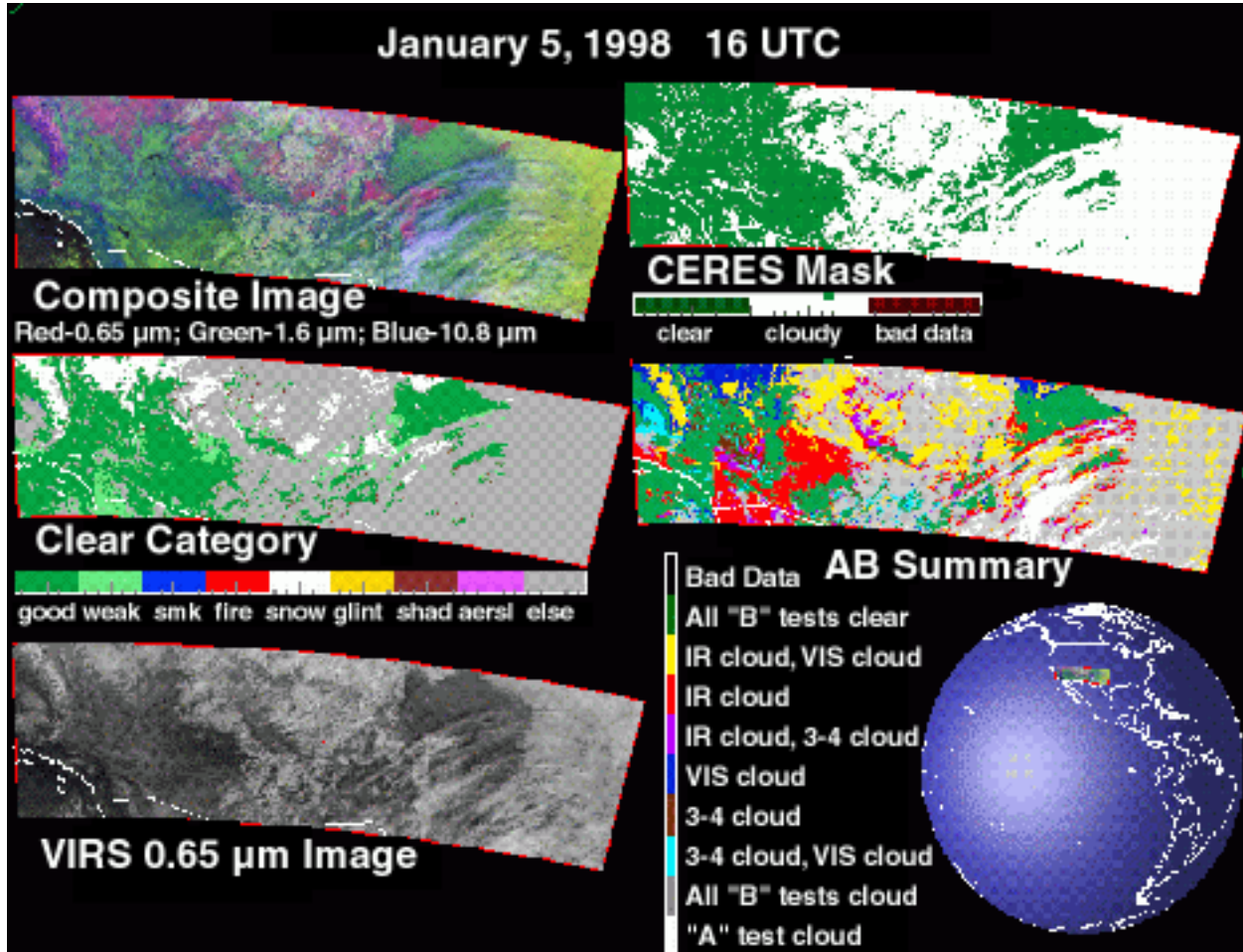*Figure 2. Example of CERES daytime cloud mask results over southwestern USA and adjacent Pacific Ocean.*

1) If $T_4 < T_{cs4} - \sigma_4$, $\qquad\qquad$ *B1* = 1.

2) If $\rho_1 > \rho_{cs1} (1 + \sigma_1)$, $\qquad\qquad$ *B2* = 1.

3) If $T_3 - T_4 > T_{cs3} - T_{cs4} + \sigma_3$, $\qquad\qquad$ *B3* = 1.

The channel-1 observed and expected clear-sky reflectances are ρ_1 and ρ_{cs1}, respectively, while σ_1 is the uncertainty in ρ_{cs1}. The observed and expected brightness temperatures for channels 3 and 4 are T_3, T_4, T_{cs3}, and T_{cs4}, respectively. The corresponding clear-sky uncertainties are σ_3 and σ_4. If the sum of the **B** parameters is 0 or 3, then the pixel is classified as either strong clear or cloudy, respectively. Otherwise, a complicated set of **C** tests is then applied depending on which **B** tests failed and on the surface type. The **C** tests adjust the clear-sky uncertainties and may also involve channels 2 or 5. For example, if the scene is bright and cold over land, the **C** test will check for snow using the expected snow reflectance ratio of 0.65 to 1.6 µm. From these **C** tests, a pixel categorized as clear may be assigned additional classifiers such as strong, weak, snow, aerosol, smoke, fire, or glint. Cloudy pixels may be classified as strong, weak, glint, or multilayered.

An example of the results of this test is shown in Figure 2 for a region over the southwestern USA. The 3-channel VIRS image shows green and bluish areas that are clear land and desert. Dark areas are clear ocean, while white, pink, and yellow areas correspond to clouds. The bright reddish areas are covered with snow. The cloud mask and clear category show that most of the clouds occur in the center and eastern half of the image with snow over the Rocky Mountains, Sierra Nevada and the western Great Plains. The **AB** summary shows examples of the various tests that were used to classify the clouds. The snowy regions were mostly yellow because the pixels passed **B** tests 1 and 2. A large part of the desert and shadowed

areas passed **B** test 1, but failed the other two. Only one small area of high clouds passed the **A** test, while many of the low clouds passed all three **B** tests (gray). The **C** tests determined whether a region that failed the **A** test remained cloudy or clear.
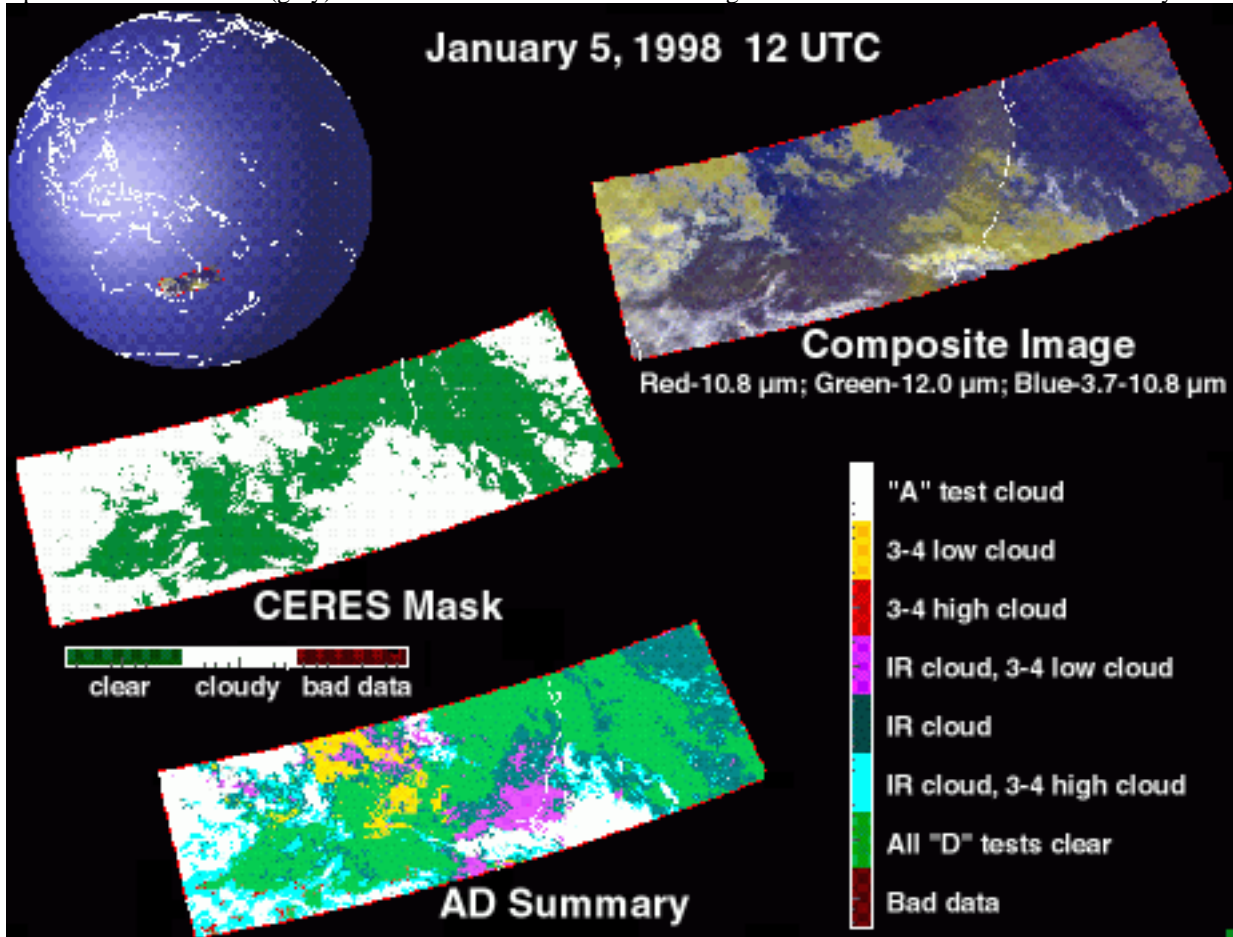

Figure 3. Example of CERES nocturnal cloud mask over the southeastern coast of Australia, 5 January 1998.

3.2 Nighttime mask

The nighttime mask is similar. The **A** test is followed by **D** tests that begin with $D1 = D2 = D3 = 0$. The **D1** and **D2** tests are the same as **B1** and **B3**, respectively. The **D3** test determines if $T_3 - T_4 < T_{cs3} - T_{cs4} - \sigma_3$. If any of the **D** tests passes, then more complex **E** tests are applied that involve refined thresholds and channel 5 radiances. Otherwise, the pixel is classified as clear. The **E** tests yield strong or weak clear or strong or weak cloudy classifications.

Figure 3 shows an example of the results of applying this mask over the southeastern coast of Australia. The three-channel infrared pseudocolor image shows relatively clear areas in blue with a mix of thick and thin high clouds that were identified with the **A** test (white in summary) and the **D2** test (light blue), respectively. The **D3** test detected some very low or sub-inversion clouds (yellow) over part of the land. Additional middle and low cloud cover was detected with the **D1** and subsequent **E** tests.

4. CLOUD PROPERTY RETRIEVAL TECHNIQUE

A set of algorithms was developed to derive cloud height z_c, optical depth, phase, effective particle size, and water path from the VIRS channels for each pixel. The main algorithm used during the daytime is the VIST (Visible Infrared Solar-Infrared Technique)[5]. Given the clear-sky radiances and surface properties for a particular set of solar zenith, viewing zenith, and relative azimuth angles, the VIST computes the spectral radiances expected for both liquid-droplet and ice-water clouds for a range of optical depths $\tau = 0.25$ to 128 for a particular cloud temperature T_c using a set of reflectance and emittance parameterizations[6]. The effective radii r_e for the model clouds range from 2 to 32 µm and the effective diameters D_e for the hexagonal ice column model clouds vary from 6 to 135 µm. The VIST matches the observed VIS, SIR, and infrared (IR; 10.8 µm) radiances to the model-computed radiances to determine which cloud properties produce the most similar combination of radiances. The process is iterative and computes results for both ice and liquid cloud particles. Phase is

determined by a combination of tests that incorporate the final cloud temperature, the initially derived cloud altitude, and a
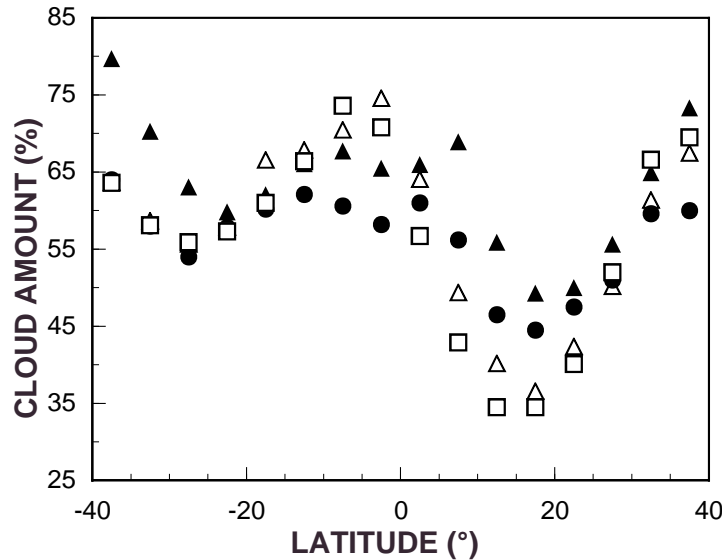
reflectance ratio of 1.6 µm to 0.65 µm. Phase selection is required to be physically reasonable. Thus, no ice clouds are
Figure 4. Mean zonal cloud amounts from VIRS for January (□) and February (○) 1998, from surface observations (●)
January 1971-81, and ISCCP D2 (▲), January 1986-93.

allowed for $T_c > 273K$ and no liquid clouds are permitted for $T_c < 233K$. Initial validation results[7,8] show that the VIST ice-cloud property retrievals are in good agreement with in situ and radar-derived values of D_e, τ, and ice water path *IWP*.

The cloud liquid water paths *LWP* and *IWP* are derived from the retrieved values of τ and particle size. Cloud-top height is the altitude or pressure from the nearest vertical temperature profile that corresponds to T_c. The cloud thickness is defined using a set of crude empirical parameterizations based on τ, T_c, and altitude. Cloud base height is defined as the difference between cloud-top height and thickness. The VIST is applied to all pixels having $\theta_o \leq 78°$. If the VIST cannot determine a solution for the observed radiances, the pixel cloud properties are listed as "no retrievals" and a second cloud mask[9] is applied to the pixel radiances to determine whether it is clear or cloudy again. If the second mask determines that the pixel is clear, then it is reclassified as a weak clear pixel. Pixels that are probably multilayered (i.e., a thin cirrus cloud over a low cloud) are identified with VIS-IR version of an overlapped cloud detection algorithm[10] and assigned a flag denoting them as overlapped. After analysis, the VIRS pixel-level results, excluding the no-retrievals, are convolved to match the corresponding CERES scanner pixel using the scanner's point spread function to weight the results. The properties are convolved according to altitude with only two layers permitted for a given CERES pixel. Four altitude layers are defined: low, 1100 to 700 hPa; low-middle, 700 - 500 hPa; high-middle, 500 - 300 hPa; and high, 300 - 50 hPa. This convolution procedure can include some higher clouds in lower layers and vice versa depending on the two cloud layers selected for the CERES pixel. The results reported here are based on averages using the convolved data.

5. RESULTS AND DISCUSSION
The mask and retrieval algorithms were applied to VIRS Version 4 data taken during January, February, and April 1998 to develop a set of preliminary results that will be used to further refine the algorithms. The VIS calibrations were found to be consistent with the latest NOAA-14 AVHRR VIS calibration[11], while nighttime comparisons of the NOAA-14 AVHRR channels 3, 4, and 5 showed consistency with their VIRS counterparts. Evaluation of the VIRS NIR channel is underway.

5.1 Cloud fraction
Including the no-retrieval pixels, the mean cloud fractions from VIRS are 58.0, 56.5, and 57.2% for January, February, and April, respectively. Over land and ocean, respectively, the mean cloud amounts were 48.9 and 59.5% during February. The mean nighttime cloud fraction was 55% compared to 58% during the daytime. These geographical and diurnal differences are similar to those from the other 2 months. During April, the **A** and **B** tests classified 40 and 42% of the daytime pixels, respectively, leaving the 18% for the more complex **C** tests. Of the daytime cloudy pixels, 90% were classified as strong cloudy. For the clear pixels, 86% were strong clear, 1.1% were classified as being shadowed, 2.9% as sunglint, and 0.2% as snow-covered.

The zonal mean cloud fractions shown in Figure 4 for January and February are very similar to those from surface[12,13] and the ISCCP climatologies[14] for January 1971-81 and 1986-93, respectively. Mean VIRS cloud amounts are very close to the surface average of 56.3%, but are considerably less than the ISCCP mean of 63.6%. The zonal variations from VIRS are

Table 1. Mean 1998 VIRS cloud properties. SC refers to supercooled liquid water.

	Ocean		Land		Desert		Total	
	Jan	Apr	Jan	Apr	Jan	Apr	Jan	Apr
z_c (km)	4.5	4.5	5.9	6.1	4.9	5.6	4.8	4.8
τ	7.3	7.7	11.9	12.0	8.4	8.3	8.2	8.6
r_e (µm)	16.2	16.6	13.1	13.3	10.6	10.2	15.6	15.9
D_e (µm)	61.8	61.9	60.3	58.9	54.7	52.2	61.3	61.1
% SC							11.4	11.6
% ice							32.7	35.0

are more extreme with a stronger maximum south of the Equator and a deeper minimum at 15°N. These extremes may reflect the effects of the strong El Nino underway during 1998.

The CERES mask is subject to further improvement as more clear-sky and bidirectional reflectance data become available. Validation efforts are continuing. The initial results are quite reasonable and will aid the development of improved cloud anisotropic models and serve as a basis for understanding the relationship between cloud properties and the radiation budget.

5.2 Cloud properties

The mean daytime cloud properties derived from VIRS are summarized in Table 1 for January and April. The results are remarkably consistent for the 2 months. Mean cloud height is roughly 1.5 km greater over land than water and lower over desert than over vegetated land. Cloud optical depths are also substantially larger over land than water, probably the result of deeper and more frequent convection over land than water. The mean cloud droplet sizes are greatest over water with an average of 16.4 µm compared to 13.2 and 10.4 µm over land and desert, respectively. Except for desert regions, the derived ice crystal sizes are apparently unaffected by the surface type. Approximately 34% of all of the observed cloud tops were categorized as ice clouds. The remaining 66% were determined to be primarily liquid water clouds and 17.4% of those were supercooled.

Figure 5a shows the variation of mean optical depth with latitude for January and April. The maxima occur around 5°S and 35°N. A slight northward shift of the tropical maximum coincides with the movement of the Intertropical Convergence Zone. Correspondingly, the maximum mean cloud heights (not shown) of 7 km are found at 5°S, while the minimum cloud height of 3.3 km occurred in the northern subtropics near 20°N close to the minimum in τ during both months. The ISCCP D2 mean optical depths for January 1986-93 have a similar zonal distribution except that the VIRS maximum is much greater. The ISCCP mean values are generally less than the corresponding VIRS averages. The discrepancy may be related to the larger cloud fraction found by ISCCP with its lower resolution (8-10 km) pixels. Although relatively constant between 30° and 60°, the VIRS-derived optical depths have a marked dependence on θ_o (Figure 5b), increasing by 40 to 70% between 60° and 78°. Much of this variation may be due to the effects of cloud structure, such as vertical inhomogeneity and small cellular fields, that are not included in the plane-parallel models used to interpret the radiances.
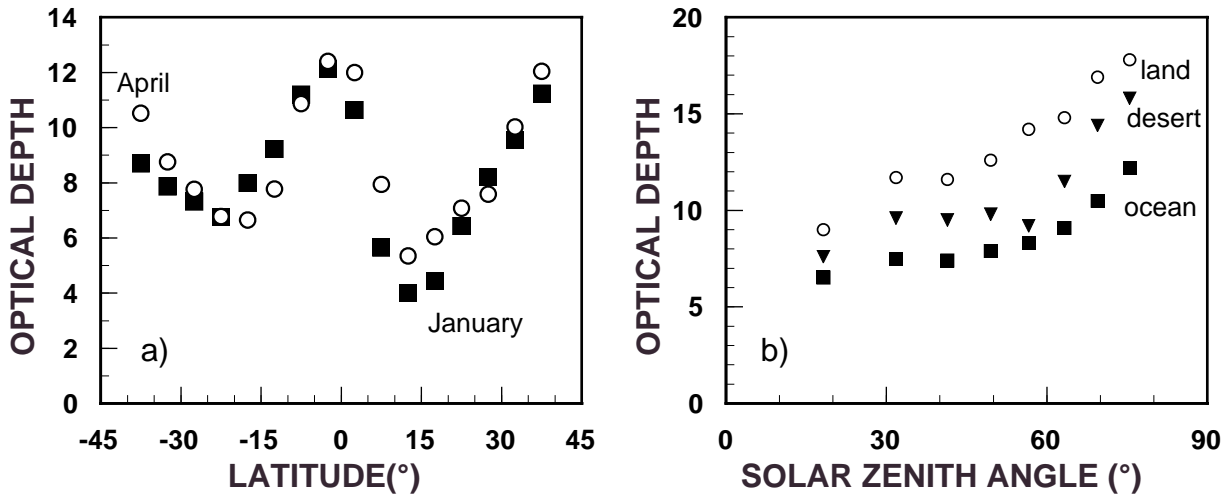
Figure 5. Variation of VIRS-derived mean optical depths with a) latitude and b) solar zenith angle (April) during 1998.
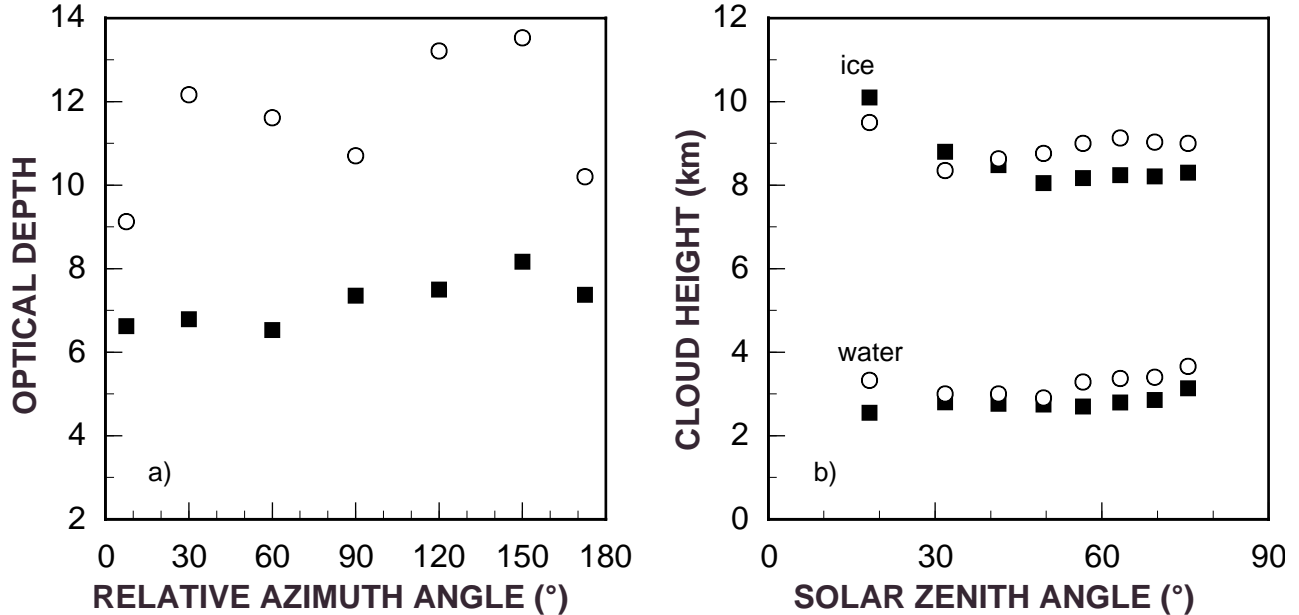

Figure 6. Variation of April 1998 (a) mean optical depths with ψ and (b) mean cloud height with θ_o. ■ – ocean, ○ –land.

The effects of cloud structure on τ were examined by computing averages as functions of θ and ψ. Minimal variation in τ occurred with θ, but the range in θ is limited by the scan angle of VIRS. The variation in ψ (Figure 6a) reveals that τ is generally larger for clouds observed in the backscattering hemisphere than from the view more toward the sun. This variation suggests that the sunlit sides of clouds are observed more when $\psi > 90°$ and shadows cast by cloud structure are observed when $\psi < 90°$. While these results confirm the expected variation of τ with ψ, additional analyses using all of the angles is required to assign some or all of the dependency in Figure 5b to the effects of cloud structure. Another factor influencing the behavior in Figure 5b may be the diurnal variation of cloud properties. It is well known that stratocumulus, which accounts for a significant part of marine cloudiness, generally thickens during the late afternoon and dissipates in the late morning. Convection over many land areas often peaks during the late afternoon, while the clearest time of day over land is often during late morning. Figure 6b indicates that over land and ocean, z_c increases with θ_o for water clouds, a result consistent with dissipation during the day and thickening during the afternoon. Ice-cloud altitude increases slightly with θ_o for land up to 60° before it levels out. The results in both Figures 5b and 6b for the smallest solar zenith angle bin should be ignored because the sampling for $\theta_o < 26°$ is confined to only half of the domain and may be geographically biased.

Figure 7 depicts the distribution of mean cloud-droplet effective radius for April 1998. The smallest droplets were found over the deserts, while the largest droplets, up to 20 µm, were observed over the open oceans on the western sides of

the oceans. However, smaller droplets on western sides of the oceans occurred off the coasts of North America, Asia, and southern Brazil. Mean droplet sizes over vegetated land areas and the stratocumulus regions off the west coasts of the continents range from 10 to 13 µm. Figure 7 is similar to the distributions of droplet sizes for January and February. The smaller values of r_e over the marine areas near most of the continental coasts relative to those over the open oceans may be the result of continental and anthropogenic aerosol effects. Additionally, the significantly smaller values over the northern midlatitude oceans ($r_e = 14.5$ µm) may be due to the transport of the anthropogenic aerosols from Asia and North America.

Although the variations of r_e with surface type are consistent with previous results from both in situ and 1987 satellite[15,16] data, the mean values exceed previous results by 18 to 25%. The Han et al.[15] data are based only on near-nadir AVHRR pixels with $T_c > 273$ K, while the Minnis et al.[16] analysis used all angles and cloud temperatures identified as liquid with no atmospheric corrections. The current analysis corrects for atmospheric attenuation and uses all liquid cloud temperatures and all angles. The NOAA-9 data were taken near 1500 local time (LT), while VIRS covers all times of day. There is essentially no dependence of r_e on θ and r_e decreases with θ_o only over land[17]. The atmospheric correction tends to decrease r_e and the values of r_e are larger for $T_c > 273$K than for colder temperatures. Thus, it is not clear why the present results differ so much from the earlier studies. These initial VIRS results were compared to coincident retrievals of cloud droplet size based on surface-based radar and microwave radiometer data[18] taken at the Atmospheric Radiation Measurement (ARM) Program Southern Great Plains (SGP) site in Oklahoma, USA between January and June 1998. The comparison uses only clouds identified as stratus with minimal overlaying high clouds near the TRMM overpass times. The satellite values of r_e were averaged over a 30 x 30-km^2 area and compared to 15-min averages from the SGP radar.
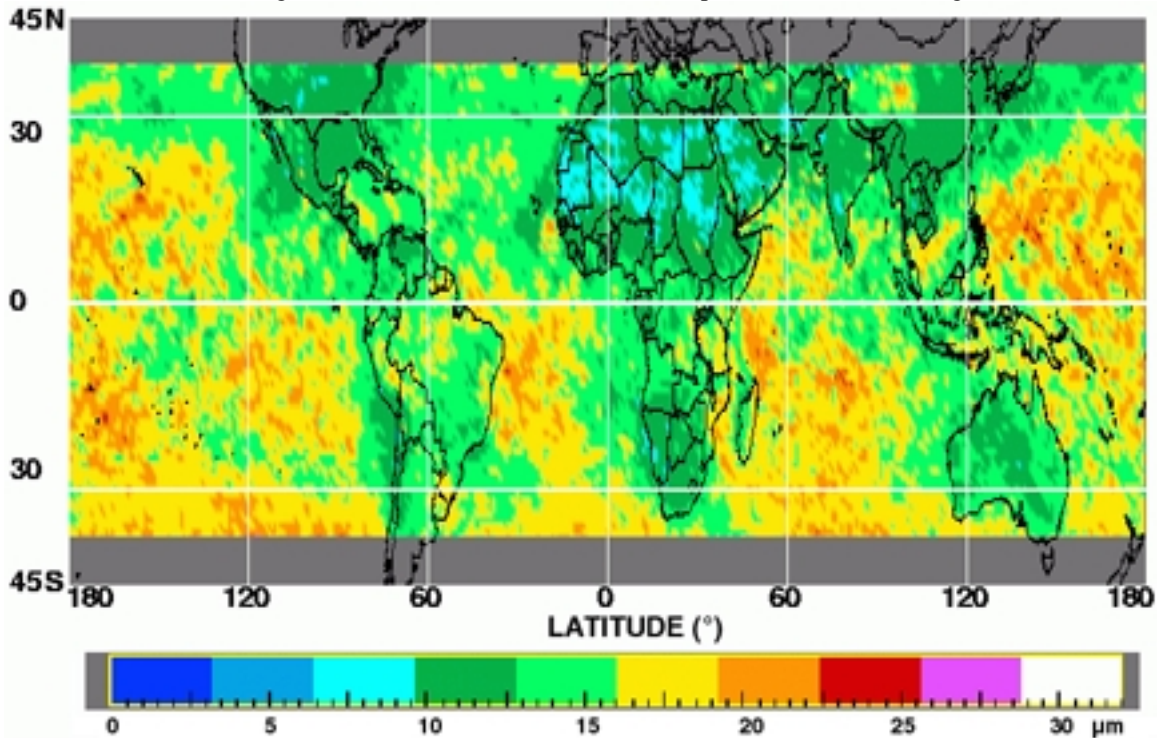

Figure 7. Mean April 1998 cloud droplet effective radius from VIRS.

The results in Figure 8 show that in some cases, r_e (VIRS) > r_e (surface), but often the two results agree well. The VIRS mean is 10.5 µm compared to the surface average of 9.2 µm. In some of the cases when the satellite radius was greater than the surface value, drizzle was evident in the radar imagery. For the scene having the greatest disagreement, some cirrus clouds were in vicinity of the ARM SGP site and contaminated the derived vale of r_e. Because ice is more absorptive than liquid water at 3.7 µm, it decreases the radiance resulting in a larger value of r_e than is present in the observed cloud. Thus, it is likely that effective particle sizes for liquid water clouds will be overestimated when cirrus clouds are in the field of view.
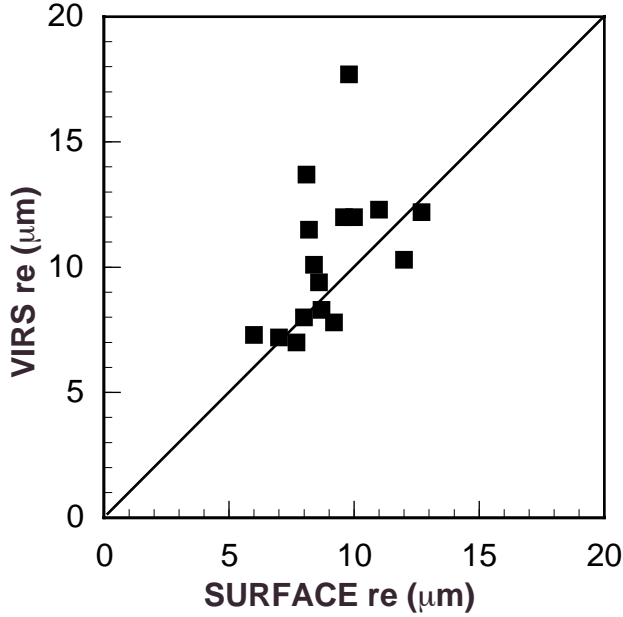

Figure 8. Surface and VIRS-derived effective radii for stratus over the ARM SGP site, January-June 1998.
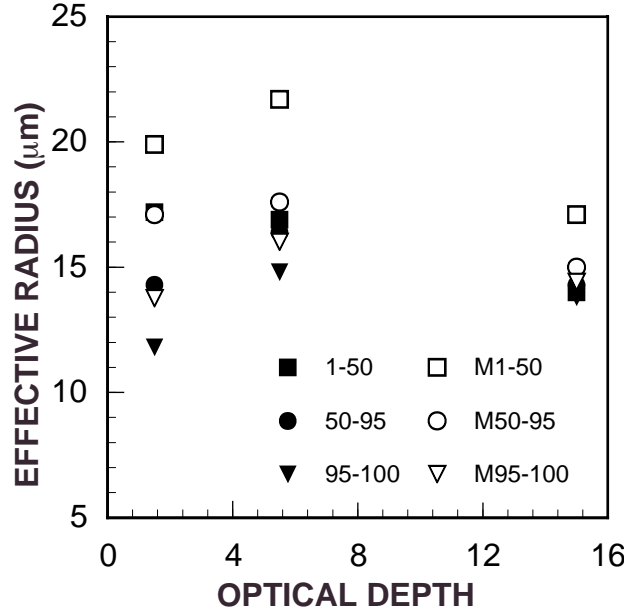

Figure 9. Mean VIRS r_e as a function of cloud amount range For single layer(solid symbols) and overlap (open symbols).
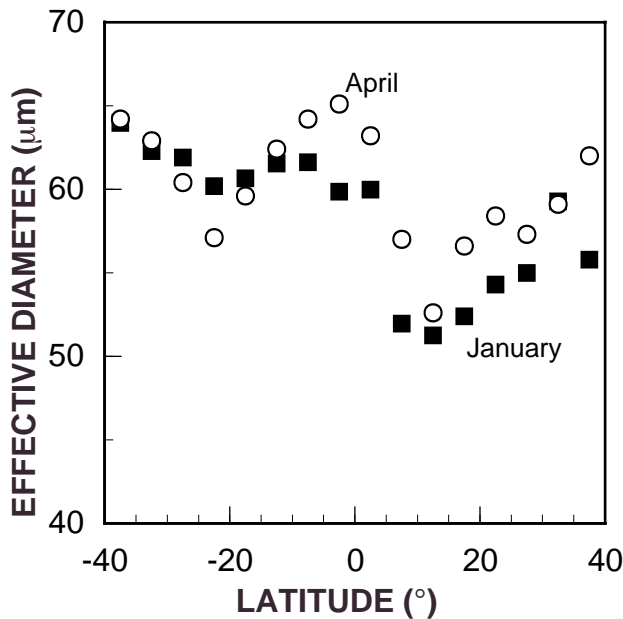

Figure 10. Mean VIRS-derived effective ice-crystal diameter for 1998.
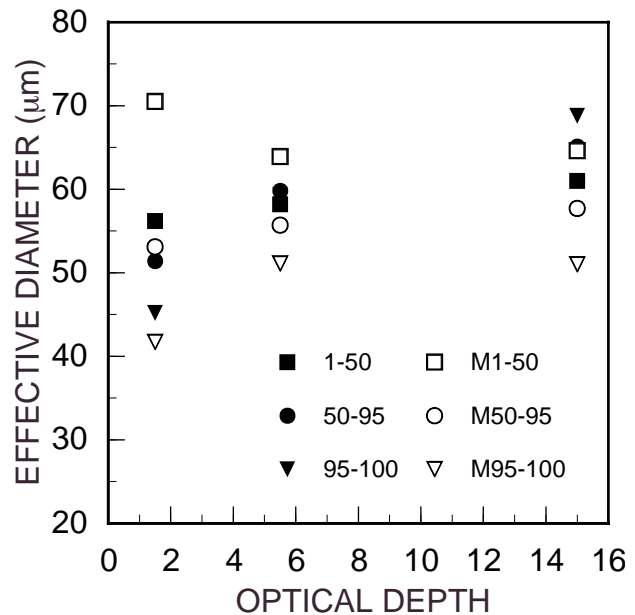

Figure 11. Mean VIRS D_e as a function of cloud amount range for single-layer (solid symbols) and overlap (open symbols).

To estimate the effect of cirrus contamination and examine the influence of cloud brokenness on the derived droplet sizes, the data were averaged in six different categories: for cloud amounts within a 1° region in the ranges of 1 - 50%, 50-

95%, and 95 – 100% for no overlapped pixels and for observations containing at least 50% overlapped cloud pixels. The results in Figure 9 show that overcast (95-100%) water droplet clouds without overlap yield the smallest values of r_e. Effective radius tends to increase with decreasing cloud fraction and is greatest for overlapped clouds. The mean value of r_e for non-overlapped overcast clouds is ~14 µm, 2 µm less than the general average (Table 1). Even for small cloud fractions, the effective radius is less than the general mean when $\tau > 10$ if no overlapped pixels are present. This figure clearly shows that many of the pixels are affected by thin cirrus contamination and that broken clouds tend to yield larger droplets. Droplet size also varies by –6% to +12% as a function of ψ, with the minima occurring at $\psi < 15°$ and $45° < \psi < 135°$ for ocean and land, respectively. The maxima occur between 165° and 180° for all surfaces. More refined segregation of the overlapped pixels and empirical corrections for broken cloud effects may be needed to account for these observed dependencies.

Another factor affecting the differences in the VIRS retrievals and earlier studies may be the effect of the channel-3 solar constant. This study uses an equivalent blackbody temperature of 355.6 K to represent the 3.7-µm solar constant. This value is based on the convolution of the VIRS filter function with the spectral solar constant and is slightly less than the 359.6K used by Minnis et al.[17] for the NOAA-9 AVHRR analyses. A comparison of the channels 3 on VIRS and the NOAA-14 or NOAA-12 AVHRRs for daylight scenes would help determine if 355.6 K is the proper value for the VIRS.

Ice crystal sizes are relatively independent of surface type (Table 1), but vary somewhat with latitude (Figure 10). The mean value of D_e is 8% larger than that from Minnis et al.[17] However, the zonal variations differ slightly with the VIRS maximum near 7°S, the location of the minimum from 1987. The deeper clouds in the Tropics (Figure 5a) may lift larger ice particles to the cloud tops than other less convective systems. The smaller crystal sizes in the Northern Hemisphere appear to be due to differences in D_e over land, possibly because of the diminished sizes over deserts (Table 1). The values of D_e over the Southern Hemisphere are 4 and 12% greater for ocean and land, respectively, than their northern counterparts. On average, D_e decreases by 4% as θ increases from 0 to 48° and D_e decreases by 11% with θ_o increasing from 0° to 78°.[17] The average ice crystal size varies by –4 to +10% with ψ and has a maximum at $\psi > 165$ and a minimum between 105° and 135°. These angular variations may be a result of the assumed ice crystal shape in the retrieval models.

Ice crystal sizes are also affected by overlapped clouds. The less absorptive droplets cause a decrease in the 3.7-µm radiance from thin ice clouds if a water cloud is underneath them. Ice particle sizes were averaged as in Figure 9 to produce the variation of D_e with optical depth, cloud fraction, and overlap shown in Figure 11. The range in mean D_e for a given optical depth is much narrower for non-overlapped clouds than for those with some overlap in the box. Ice crystal size appears to increase with τ, perhaps for the reasons noted earlier for deep convection, and is smallest for thin overcast clouds. This variation may also explain why the subtropics have the lowest values of D_e. The effect of cloud overlap is most prominent for scenes with optically thick clouds.

6. CONCLUDING REMARKS

The initial results from the CERES analysis of VIRS are generally consistent with previous retrievals of cloud properties from satellite measurements and with the current understanding of the diurnal cycles of clouds. Validation of the results is underway using surface observations taken in the Tropics and midlatitudes. This new data set contains an unprecedented variety of cloud property information that will require careful dissection and analysis. Much closer examination of the results is needed to understand the reasons for disagreements with previous measurements and the observed angular dependencies. More refined techniques could then be developed to overcome some of the shortcomings. Additional algorithms are under development to improve the phase and particle size retrievals using the 1.6-µm channel[19] and to attempt retrievals of cloud properties more accurately for overlapped conditions. An improved technique for detecting and analyzing the properties of thin clouds at night is also under development and will be implemented to achieve consistency in the retrieved cloud fields over the entire diurnal cycle. The VIRS cloud properties, however, can already aid the goal of improved interpretation of CERES radiances and determination of the interaction between clouds and the radiation budget.

7. ACKNOWLEDGEMENTS

8. REFERENCES

1. Wielicki, B. A., B. R. Barkstrom, B. A. Baum, T. P. Charlock, R. N. Green, D. P. Kratz, et al.: "Clouds and the Earth's Radiant Energy System (CERES): Algorithm overview," IEEE Trans. Geosci. Remote Sens., **36**, pp. 1127-1141, 1998.

2. Sun-Mack, S., Y. Chen, T. D. Murray, P. Minnis, and D. F. Young, "Visible clear-sky and near-infrared surface albedos derived from VIRS data for CERES", *Proc. AMS 10th Conf. Atmos. Rad.*, Madison, WI, June 28-July 2, pp. 422-425, 1999.

3. Minnis, P. and E. F. Harrison, "Diurnal variability of regional cloud and clear-sky radiative parameters derived from GOES data. Part III: November 1978 radiative parameters", J. Climate Appl. Meteor., **23**, pp. 1032-1052, 1984.

4. Minnis, P., W. L. Smith, Jr., and D. F. Young, "Surface emissivity derived from multispectral satellite data", *Proc. 8th Ann. ARM Science Team Mtg.*, Tuscon, AZ, March 23-27, pp. 489-494, 1998.

5. Minnis, P., D. P. Kratz, J. A. Coakley, Jr., M. D. King, D. Garber, P. Heck, S. Mayor, D. F. Young, and R. Arduini, "Cloud Optical Property Retrieval (Subsystem 4.3). Clouds and the Earth's Radiant Energy System (CERES) algorithm theoretical basis document, Volume III: Cloud Analyses and Radiance Inversions (Subsystem 4)", *NASA RP 1376 Vol. 3*, pp. 135-176, 1995.

6. Minnis, P., D. P. Garber, D. F. Young, R. F. Arduini, and Y. Takano, "Parameterization of reflectance and effective emittance for satellite remote sensing of cloud properties", J. Atmos. Sci., **55**, pp. 3313-3339, 1998.

7. Young, D. F., P. Minnis, D. Baumgardner, and H. Gerber, "Comparison of in situ and satellite-derived cloud properties during SUCCESS", Geophys. Res. Lett., **25**, pp. 1125-1128, 1998.

8. Mace, G. G., T. P. Ackerman, P. Minnis, and D. F. Young, "Cirrus layer microphysical properties derived from surface-based millimeter radar and infrared interferometer data", J. Geophys. Res., **103**, pp. 23,207-23,216, 1998.

9. Welch, R. M., S. K. Sengupta, A. K. Goroch, R. Palikonda, N. Rangaraj, and M. S. Navar, "Polar cloud and surface classification using AVHRR imagery-An intercomparison of methods", J. Appl. Meteorol., **31**, pp. 405-420, 1992.

10. Baum, B. A., P. Yang, and A. Heymsfield, "Overlapping cloud layer detection and analysis using MODIS Airborne Simulator imagery", *Proc. AMS 10th Conf. Atmos. Rad.*, Madison, WI, June 28-July 2, pp. 230-233, 1999.

11. Nguyen, L., P. Minnis, J. K. Ayers, W. L. Smith, Jr., and S.-P. Ho, "Intercalibration of geostationary and polar satellite imager data using AVHRR, VIRS, and ATSR-2 data", *Proc. AMS 10th Conf. Atmos. Rad.*, Madison, WI, June 28-July 2, pp. 405-408, 1999.

12. Warren, S.G., C.J. Hahn, J. London, R.M. Chervin, and R.L. Jenne, "Global distribution of total cloud cover and cloud type amounts over land", *NCAR Tech. Note NCAR/TN-273+STR*, 229 pp., 1986.

13. Warren, S.G., C. J. Hahn, J. London, R.M. Chervin, and R. L. Jenne, "Global distribution of total cloud cover and cloud type amounts over ocean", *NCAR Tech. Note NCAR/TN-317+STR*, 212 pp., 1988.

14. Rossow, W. B. and R. A. Schiffer, "ISCCP cloud data products", Bull. Am. Meteor. Soc., **72**, pp. 2-20, 1991.

15. Han, Q., W. B. Rossow, and A. A. Lacis, "Near-global survey of effective drop radii in liquid water clouds using ISCCP data", J. Climate, **7**, pp. 465-497, 1994.

16. Minnis, P., D. F. Young, B. A. Baum, P. W. Heck, and S. Mayor, "A near-global analysis of cloud microphysical properties using multispectral AVHRR data", *Proc. AMS 9th Conf. Atmos. Radiation*, Long Beach, CA, Feb. 2-7, pp. 443-446, 1997.

17. Minnis, P., D. F. Young, B. A. Wielicki, P. W. Heck, S. Sun-Mack, and T. D. Murray, "Cloud properties derived from VIRS for CERES", *Proc. AMS 10th Conf. Atmos. Rad.*, 28 June - 2 July, Madison, WI, pp. 21-24, 1999.

18. Dong, X., P. Minnis, S. Sun-Mack, G.G. Mace, and E. E. Clothiaux, "Validation of CERES/VIRS cloud property retrievals using ground-based measurements obtained at the DOE ARM sites", *Proc. AMS 10th Conf. Atmos. Rad.*, 28 June - 2 July, Madison, WI, pp. 29-32, 1999.

19. Young, D. F, P. Minnis, and R. F. Arduini, "A comparison of cloud microphysical properties derived using VIRS 3.7 µm and 1.6 µm data", *Proc. AMS 10th Conf. Atmos. Rad.*, 28 June - 2 July, Madison, WI, pp. 25-28, 1999.